Tracking the Early-life of PtNi/C Shape-Controlled Catalysts upon their Integration in PEMFC

Camille Roiron, Masuma Sultana Ripa, Lisa Pierinet, Frédéric Charlot, Frédéric Maillard, Sylvain Brimaud, Laetitia Dubau

Tracking the Early-life of PtNi/C Shape-Controlled Catalysts upon their Integration in PEMFC

Camille Roiron[a], Masuma Sultana Ripa[b], Lisa Pierinet[c], Frédéric Charlot[d], Frédéric Maillard[a], Sylvain Brimaud[bz] Laetitia Dubau[az]

[a] Univ. Grenoble Alpes, Univ. Savoie Mont Blanc, CNRS, Grenoble INP, LEPMI, 38000 Grenoble, France.
[b]Zentrum für Sonnenenergie- und Wasserstoff-Forschung Baden-Württemberg (ZSW), Helmholtzstrasse 8, 89081 Ulm, Germany
[c] Symbio, 5 rue Simone Veil, 69200 Venissieux, France
[d] Univ. Grenoble Alpes, Grenoble INP, CMTC, 38000 Grenoble, France

[z]Laetitia Dubau [laetitia.dubau@grenoble-inp.fr]
Sylvain Brimaud [sylvain.brimaud@zsw-bw.de]

Abstract

The integration of promising bimetallic electrocatalytic active materials for oxygen reduction reaction (ORR) into practical and functional proton-exchange membrane fuel cell (PEMFC) electrodes remains largely impeded by the poor performances that these exhibit at high current loads. The early life of PtNi/C catalysts presenting either structurally faceted/ordered or defective/disordered surface morphology is compared to that of both spherical PtNi/C and Pt/C catalysts. Different single-cell operating conditions were studied. At low current density, in the kinetically limited region, a good agreement between liquid electrolyte and single-cell configuration is reported and the kinetic benefit of PtNi/C catalysts compared to Pt/C is (at least partially) maintained. However, PtNi/C catalysts show severe limitations in the O_2 mass transport limited region. Morphological and compositional changes were monitored at each stage showing that Ni atoms are leached at every step from ink formulation to the first PEMFC test. We show that Ni is already redistributed in the membrane in the fresh membrane electrode assembly (MEA) state. Ni^{2+} cationic contamination of the ionomer/membrane contributes to the disappointing results obtained in MEA configuration. In addition, for shaped-controlled PtNi/C, the surface faceting loss combined with restructuring via coalescence and crystallite growth further compromise their transfer in technological devices.

Introduction

Hydrogen fuel cell vehicles are considered an alternative to decarbonized power trains for heavy-duty transportation. Proton exchange membrane fuel cell (PEMFC) is the most technologically advanced device converting the chemical energy of hydrogen into electricity with characteristics fitted for transportation. To maximize their durability, PEMFC should operate at high potential, thus increasing the need for a cathode catalyst able to lower the oxygen reduction reaction (ORR) overpotential. Minimizing the use of platinum (Pt) is essential to ensure the long-term sustainability of PEMFC technology deployment. For over three decades, Pt-transition metal alloys/C have been considered viable alternatives to pure Pt/C catalysts in catalyzing the ORR. Notably, Pt_xM alloys (where M = nickel (Ni), cobalt (Co), or copper (Cu)) share the same crystallographic space group as pure Pt, exhibiting a face-centered cubic phase where 1/(1+x) of Pt atoms are being replaced by smaller transition metal atoms. Alloying Pt with smaller elements induces a beneficial strain effect, contracting the Pt lattice and weakening the binding energy of ORR intermediates[1,2]. In addition, the presence of an alloying element modifies the electronic properties of the surrounding Pt atoms, known as the ligand effect[3–5]. For example, a Pt_3Ni (111) surface demonstrates a 10 times higher ORR activity than Pt (111)[3]. For a given Pt loading on the electrode, Pt alloys present higher activity toward the ORR, especially when measured in contact with an aqueous liquid electrolyte. Performance improvement is quantified using the current density enhancement factor (EF) compared to a reference Pt/C catalyst for different testing conditions at various potentials. To further improve the ORR activity of Pt-alloys, two strategies are implemented[2,6]. The first one is to expose preferentially the Pt_3M (111) facets which have been proven to be the most active in single-crystal experiments[3]. At the nanometer scale, PtNi/C Octahedra and Icosahedra nanoparticles presenting only (111) facets were proven to have substantially higher specific activity than spherical Pt/C nanoparticles[7–15]. Up to a 10-fold increase of both mass and specific activity have been reported for octahedra Pt_3Ni/C compared to Pt/C nanoparticles[7]. Recently, it has also been reported that highly defective PtNi/C catalysts exhibit improved ORR activity compared to PtNi Spheres [6,8,16–18]. For instance, an enhancement factor (EF) of 9 of the ORR activity at 0.95 V has been reported for highly defective Sponge Pt_3Ni/C compared to Pt/C[2]. In the case of disordered catalysts, the broad strain distribution creates highly active sites interspersed among less active ones.

However, transferring the high EF monitored in liquid electrolyte to the more practical and complex technological electrodes used in membrane electrode assembly (MEA) configuration has proven challenging, particularly for shape-controlled Pt-alloy/C catalysts[19–22]. One of the

main hindering factors to their implementation in realistic devices is the dissolution of transition metals in the harsh acidic and oxidative conditions of the PEMFC cathode. This *in situ* dissolution has been reported for PtNi/C and PtCo/C alloys (PtCu/C being rarely studied) and several aging studies report drastic performance loss at high current density[23–28]. Metal dissolution causes oxygen transport limitations, as revealed by limiting current measurements under various oxygen (O_2) concentrations[22,23,29]. Very recently, transition metal contamination of the cathode catalytic layer has been precisely studied, revealing how the protons of the sulfonic groups of the ionomer are quickly replaced by transition metals cationic species, hindering their water uptake properties, resulting in detrimental oxygen transport properties[26,27,30–34]. Transition metal concentration is homogenized in the ionomer phase (thin film and bulk membrane) when temperature or relative humidity is increased[24,27,32]. Interestingly, a threshold of transition metal content under which transport properties are almost unaffected has been reported [26,30]. The corresponding amount of transition metal and the absolute value of this threshold depend on the total amount of sulfonate groups in the ionomer phase (*i.e.* I/C value, the equivalent weight of the ionomer, membrane thickness, and total volume of membrane present), as well as on the dissolved ion valence and size[26,27,31].

Some previous contributions[21,22,24,30,35] mentioned losses in the second metal in the MEA state compared to the catalyst powder. One publication even proceeds to acid wash the prepared MEA to avoid beginning-of-life contamination[28]. Yet, in these works, the process occurring at each step of the MEA fabrication is not studied. A systematic and model investigation tackling a quantitative assessment of these losses and their consequences at the material level and on functional electrode properties, which encompasses the whole PEMFC electrode manufacturing process and testing, is still lacking. In particular, the beginning of life morphological, structural, and compositional changes of different PtNi/C nanoparticles structure/shape transferred into MEA are still overlooked in the literature and are the focus of the present study. This work is based on a library of highly active ORR catalysts (faceted, disordered, and spherical nanoparticles), as well as a Pt/C reference catalyst. Our group has studied the extent of Pt and Ni dissolution during accelerated stress testing using online inductively coupled plasma mass spectrometry for the same series of materials[36]. To ensure a fair comparison, all catalysts were supported on the same Vulcan XC72 substrate. Herein, we track changes in the composition and structure of the various Pt/C and PtNi/C catalysts throughout their integration into a PEMFC device. The analysis spans from material synthesis to the end of the first

electrochemical testing (first polarization curve measurement), encompassing the ink formulation and the break-in procedure.

Experimental

Three types of PtNi/C catalysts with different shapes were integrated into 25 cm² MEAs and their performance was compared to that of a monometallic Pt/C catalyst. Two in-house Pt_xNi/C ($2 < x < 3$) catalysts with octahedral and 'sea sponge' particle shapes were synthesized. They are referred to as PtNi/C Octahedron and PtNi/C Sponge, respectively. Additionally, two spherical-shaped catalysts, one with and one without Ni, were used as commercial references: they are referred to as PtNi/C Sphere and Pt/C Sphere, respectively. Representative transmission electron microscopy (TEM) images of the different materials are displayed in ***Figure 1a,*** and the synthesis protocol and particles' composition are fully described in the ***Supplementary Information***. The morphology, composition, and ORR activity of the catalysts in aqueous liquid electrolyte have been determined at various stages during their integration within MEAs (the MEA fabrication procedure is thoroughly described in the ***Supplementary Information*)**. The as-synthesized catalyst, designated as "Powder", was dispersed in a mixture of water, ethanol, and ionomer solution and was spray-deposited on a commercial proton-exchange membrane (PEM) containing a Pt layer as a peroxide scavenger. The Pt/C Sphere catalyst layer for the anode was deposited using the same method. The obtained anode and cathode catalyst layers sandwiching the PEM are designated as "Fresh MEA". In this collaborative project, the MEAs were fabricated in two different laboratories (ZSW and Symbio) using similar protocols for manufacturing cathode catalyst layers. The anode catalyst layers loading, assembly process, and break-in procedures employed varied between the two laboratories, each following the standardized internal processes. The two sets of MEAs prepared at ZSW and Symbio are later designated as MEA_{ZSW} and MEA_{Symbio}, respectively. The protocols used in both laboratories are fully described in the ***Supplementary Information***. Briefly, three polarization curves are recorded in H_2/air at 80°C at different RH and O_2 stoichiometry. After the conditioning stage and the measurement of the three polarization curves, the cathodic catalyst layer was scrapped and designated as "Tested MEA".

The fuel cell polarization curves show similar performance for the sets of MEAs from both laboratories (RH range: 35-100%, O_2 stoichiometry range: 1.6-3, comparison of the data presented in ***Figure 1*** and ***Supplementary Figure 2***). This suggests that results can be obtained independently from MEAs prepared and tested in either laboratory.

Results

Performance of PtNi/C catalysts in membrane electrode assembly

The catalyst's performance in single-cell configuration was evaluated under varying conditions of O_2 stoichiometry and relative humidity (RH). The polarization curves recorded for each material with the highest O_2 stoichiometry and RH (stoichiometry 3 and 100% RH) are displayed in ***Figure 1b***. The measurements for all other conditions conducted in the two laboratories are displayed in ***Supplementary Figures 2*** and ***Supplementary Figures 3***. As the measured high-frequency resistance (HFR) was identical for all the MEAs incorporating these different catalyst materials, the polarization curves were not corrected from HFR (see the impedance data provided in ***Supplementary Figure 1***). We note that PtNi/C Sponge and PtNi/C Octahedron perform better than the benchmark Pt/C Sphere at current densities lower than 1 A cm^{-2}_{geo} (or cell voltages lower than 0.7 V). However, there's a noticeable decline in performance when subjected to current density exceeding 1 A cm^{-2}_{geo}. To compare the catalytic performance obtained in solid (MEA configuration) and liquid electrolytes, the ORR mass activities at 0.9 V have been calculated (current at 0.9 V normalized by Pt loading) and are displayed in ***Figure 1c***. It is worth noting that, in liquid electrolyte, the 3-electrode system allows for a measurement of the potential *vs* the reversible hydrogen electrode (*E*) whereas, in MEA configuration, 0.9 V corresponds to the cell voltage (*U*). The MEA values are averaged over the two sets of independent measurements. For all the materials (with or without Ni), the mass activity obtained in PEMFC is lower than that obtained in liquid electrolyte. The lower activity in the MEA configuration can be attributed to a lower utilization factor of the catalysts in the cathode catalyst layer[37,38] but also to the crossover of H_2 and its oxidation at the cathode, resulting in the decrease of both cathode potential and current measured.

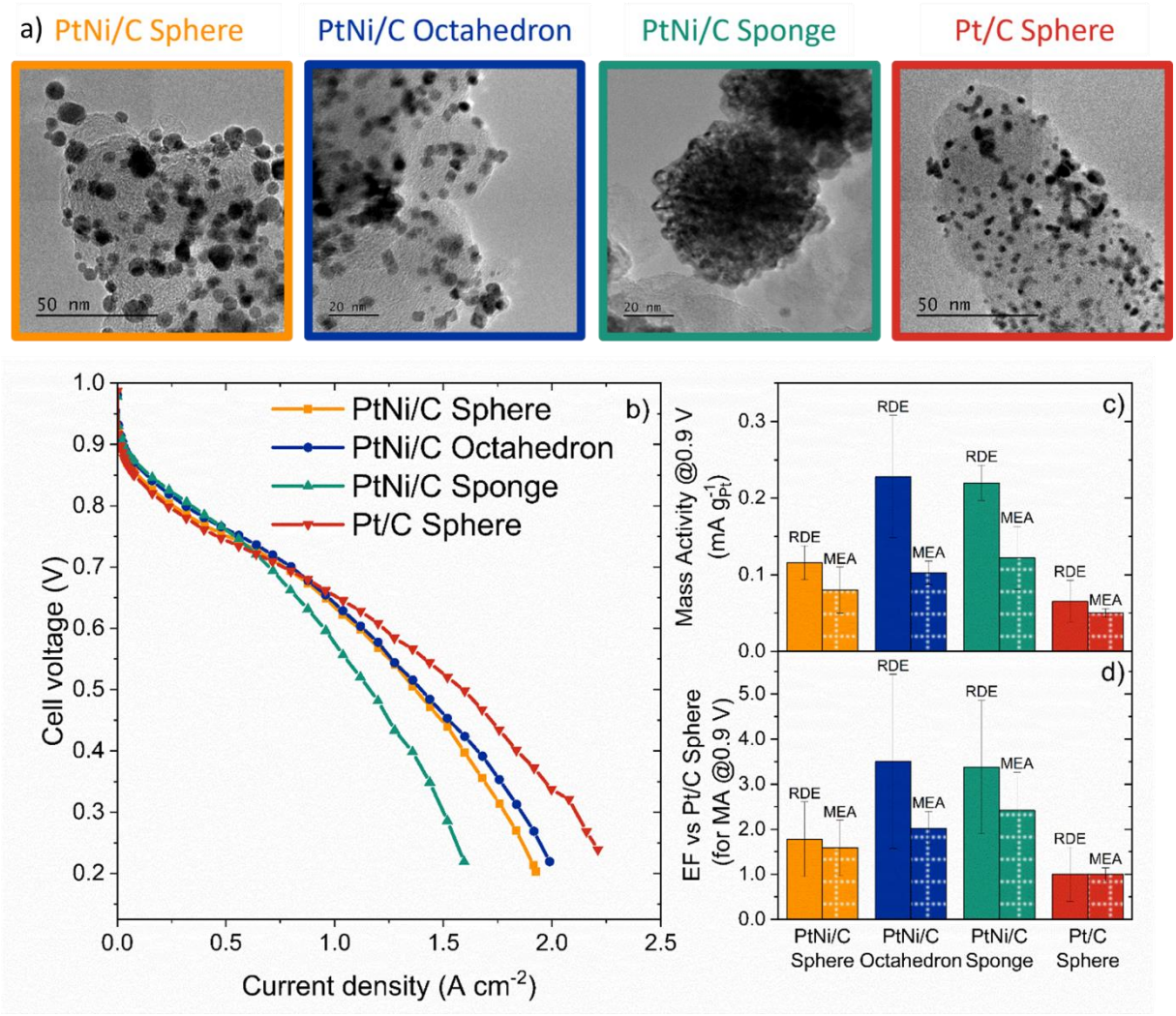

Figure 1 - a) Transmission electron microscopy images from the library of materials used in this study with same magnification, b) Low current zoom-in of 25 cm² MEA polarization curve recorded at 80 C, 100% RH, 1.5barg in H_2/Air, c) Mass activity of the catalyst at 0.9 V in RDE and MEA set-up (recorded at 80 °C, 100% RH, 1.5barg in H_2/Air) averaged over the two sets of measurements. d) Enhancement Factor (EF) vs. benchmark Pt/C Sphere catalyst in each set-up: ORR mass activity of the catalyst at 0.9 V divided by that of the Pt/C reference catalyst for both MEA and liquid electrolyte (RDE) characterization (RDE at 25 °C, 1600 rpm in 0.1 M $HClO_4$ and MEA at 80 °C and 1.5 barg).

To assess the impact of MEA integration on the various catalysts examined in this study, the enhancement factors (EF) in mass activity at E = 0.9 V and U = 0.9 V for both RDE and MEA set-ups are displayed in ***Figure 1d***. The EF of PtNi/C Sponge and PtNi/C Octahedron decreases upon integration in MEA. This suggests that either: i) the utilization factor of the bimetallic catalysts is lower, due to a modified structure of the catalyst layer or ii) the catalyst surface undergoes modification upon integration into an MEA, resulting in lower intrinsic ORR

activity. For a more detailed analysis of these decays of EF at low current density, the influence of the RH and O_2 stoichiometry was investigated (see the polarization curves presented in ***Supplementary Figure 2***). The selected metrics in ***Figure 2a*** and ***Figure 2b*** for comparing MEA performance are the power density measured at U = 0.9 V (±0.005 V) for the low current densities (ranging from 0.015 to 0.032 A cm^{-2}_{geo}) and the power density measured near 1.52 A cm^{-2} for the high current densities. In ***Figure 2-a***, we note that increasing the RH enhances the performance of MEAs embedding PtNi/C Octahedron and PtNi/C Sponge. In the driest conditions, lower performance is observed, approaching that of the benchmark PtNi/C Sphere and Pt/C Sphere (for which RH does not influence the performance). The power density at 1.52 A cm^{-2} as a function of the O_2 stoichiometry at the cathode for the four materials is displayed in ***Figure 2-b***. At such current density, the hydration of the layer is regulated by the water generated through the ORR, rather than by RH. As expected, an increase in the O_2 stoichiometry improves the performance of all the materials. Yet, the effect of increasing the O_2 stoichiometry on the improvement of the MEAs performance varies depending on the catalyst material incorporated in the cathode catalyst layer, following the order Pt/C Sphere < PtNi/C Sphere < PtNi/C Octahedron << PtNi/C Sponge. To investigate the transport properties of the cathode catalyst layers, both O_2 and H^+ transport resistances were measured after acquiring the polarization curves. The O_2 transport resistance of the cathode catalyst layer was determined using limiting current measurement, following the method described by Mashio et al. [39]. A detailed description of the measurement procedure can be found in ***Supporting Information***. The O_2 transport resistance comprises two components: a pressure-dependent resistance, which pertains to O_2 transport within the gas diffusion layer-microporous layer (GDL-MPL), and a pressure-independent resistance, which assesses O_2 accessibility to the active sites within the catalyst layer. These two contributions are reported in ***Figure 2c*** for MEA_{ZSW}. The pressure-independent resistance from MEA_{Symbio} is reported in ***Supplementary Figure 4*** for the other set of measurements. As expected, the pressure-dependent O_2 resistance remains consistent across all four materials, in line with identical GDL-MPL employed in MEA testing. However, the local O_2 transport resistance is very different from one catalyst layer to another. The reference Pt/C Sphere material exhibits the lowest O_2 transport resistance whereas it triples for the PtNi/C Sphere and PtNi/C Octahedron and quadruples for the PtNi/C Sponge.

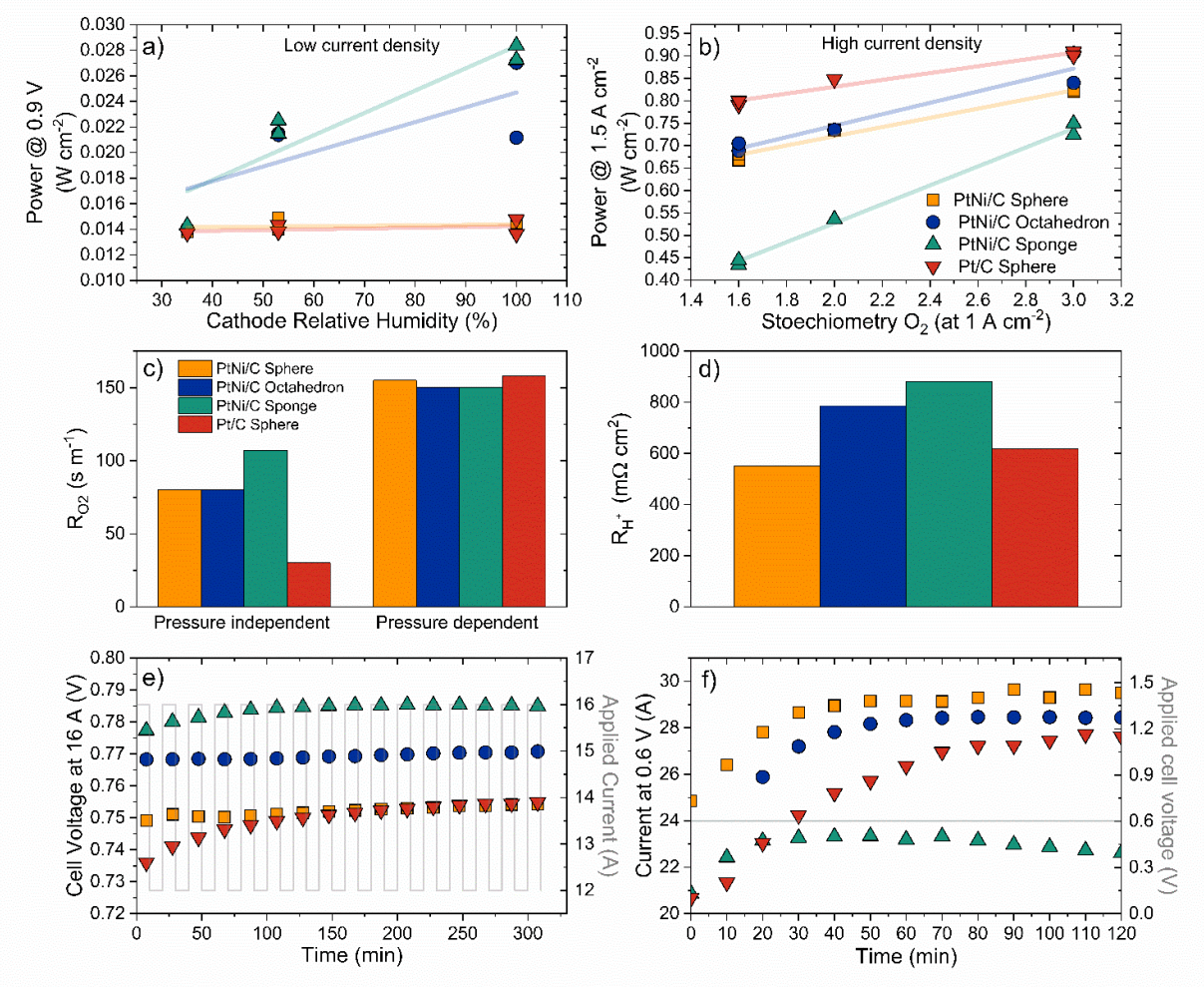

Figure 1 - a) Power density recorded at U = 0.9 V as a function of the cathode relative humidity b) Power density recorded at 1.5 A cm^{-2}_{geo} as a function of the oxygen stoichiometry at 1 A cm^{-2} for the MEA_{ZSW} c) Pressure-dependent and pressure-independent oxygen transport resistance measured at 80 °C, 100 % RH and d) Proton transport resistance measured for each MEA at the end of the test under H_2/N_2 (anode/cathode) at 60% RH, 80 °C - Evolution of PEMFC performance during two types of activation procedures. e) For MEA_{ZSW}: 10 min current steps at 12 and 16 A (0.48 and 0.64 A cm^{-2}) applied for 322 min and f) For MEA_{Symbio}: Potential hold at 0.7 V for 120 min.

The values of the proton transport resistance within the cathode catalyst layers, measured from electrochemical impedance spectroscopy under H_2/N_2 (anode/cathode) at 60% RH, are reported in ***Figure 2f***. A detailed description of the measurement procedure is provided in the ***Supporting Information***. For cathode catalyst layers incorporating PtNi/C Octahedron and PtNi/C Sponge, the proton transport resistance is increased by 27% and 43% respectively compared to that of Pt/C Sphere. However, the proton transport resistance is 10% smaller for the PtNi/C Sphere than that of the Pt/C Spheres.

The conditioning (break-in) of the MEAs incorporating the four materials investigated in this study, one under current load control and the other under cell voltage control, are presented in ***Figure 2e*** and ***Figure 2f***, respectively. Classically, break-in procedures aim to achieve high and stable MEA performance by ensuring a stable hydration state of the ionomer of the catalyst layer and the membrane, thus ensuring good protonic conductivity, and clean chemical impurities from the surface of the catalysts through oxidative removal. The first protocol involves alternating 10-minute current steps of 12 and 16 A (0.48 and 0.64 A cm^{-2}_{geo}, respectively) for 320 min. The evolution of the cell voltage over time, measured at the end of each 16 A step, is represented in ***Figure 2e.*** The cell voltages at 16 A at the end of the break-in procedure are ranked as follows: Pt/C Sphere ≈ PtNi/C Sphere (0.755 V) < PtNi/C Octahedron (0.771 V) < PtNi/C Sponge (0.785 V). The second protocol entails a steady voltage hold at $U = 0.6$ V for 2 hours. The current values averaged over 10 minutes are represented in ***Figure 2f***. They rank as follows: PtNi/C Sponge (22.6 A) < Pt/C Spheres (27.6 A) < PtNi/C Octahedron (28.4 A) < PtNi/C Sphere (29.5 A). The different ranking obtained with the two different protocols is explained by the evolution of the relative performance of the MEAs between the two operating points considered. In both cases, the activation is more beneficial for the Pt/C catalysts. For the nickel-containing materials, the catalyst layer properties seem to evolve during the activation protocol, thereby impeding performance improvement. To investigate the phenomenon at place during the integration of these catalysts into MEA, the properties of the catalyst materials are monitored through the membrane assembly fabrication and testing.

Evolution of ORR catalyst chemical and structural properties during MEA fabrication and characterization

The morphology and the particle size of the catalysts present in the Fresh and Tested MEA can be compared to those of the pristine Powders using TEM. The TEM images displayed in ***Figure 3*** illustrate changes in morphology for PtNi/C Octahedron and PtNi/C Sponge catalysts. Specifically, the distinct octahedral shape is gradually lost following both MEA manufacturing and MEA testing. The loss of (111) facets in the octahedron structure is expected to harm the ORR activity, as it entails the disappearance of highly active (111) facets characteristic of the octahedron structure[7]. The morphology of the Sponge PtNi/C catalyst remains intact during the MEA manufacturing (from pristine Powder to the freshly prepared MEA). However, after the electrochemical testing, the individual crystallites have coalesced/merged, resulting in a less porous structure comprising larger crystallites. The particle size distribution at each

incorporation stage into MEAs is displayed in ***Supplementary Figure 5***. The change in particle size distribution is negligible for the spherical nanoparticles, as expected for these structures when they do not experience durability tests or accelerated degradation tests. For the PtNi/C Octahedron, the loss of morphology is accompanied by a flattening of the particle size distribution, with the presence of small particles and big agglomerates consequential to the merging of particles. For PtNi/C Sponge, crystallite agglomeration cannot be quantified, and the particle diameter measured corresponds to the agglomerated structure. The size of the agglomerate seems to be decreasing upon incorporation in the MEA, possibly because of the loss of porosity caused by the crystallite size increase.

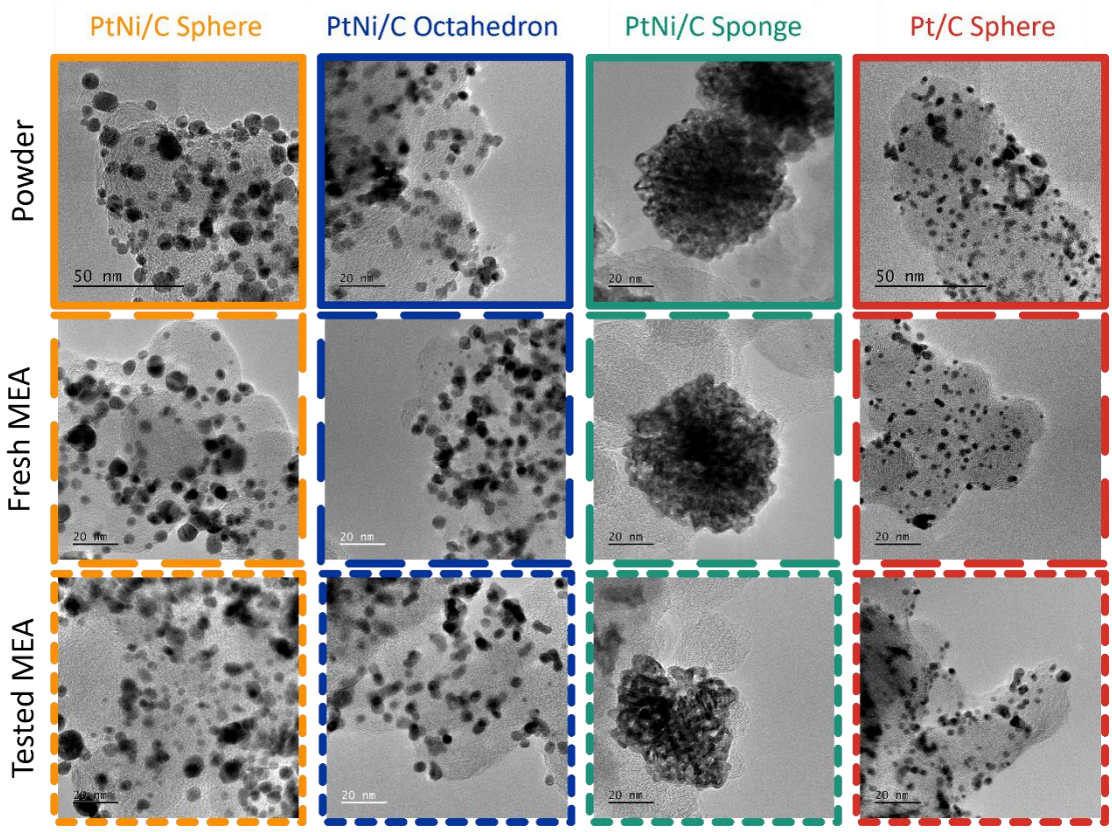

Figure 3 - Transmission electron microscopy images in the pristine powder state (Powder), after deposition on the PEM (Fresh MEA) and after beginning-of-life testing (Tested MEA) of the MEA_{Symbio}.

The Pt/Ni atomic ratio was tracked for all samples at each stage from the pristine Powder to the Tested MEA, using energy-dispersive X-ray spectroscopy coupled with transmission electron microscopy (TEM-EDX), see ***Figure 4a.*** Remarkably, between 16 and 30 % of the initial present Ni is dissolved during the formulation of the catalyst ink. For PtNi/C Sponge, the synthesis ends with an acid leaching step to remove Ni, but the ink formulation still causes

additional nickel dissolution. This suggests that the catalytic ink preparation leads to a more pronounced dissolution of Ni compared to the acid-leaching process. In a side experiment, we evaluated the influence of the ink composition on the extent of Ni leaching for the powder PtNi/C Octahedron. Different ionomer and water-to-catalyst ratios have been tested. As shown by ***Supplementary Figure 6***, the presence of Nafion increases the Ni loss, as does a significant quantity of water. Thus, we conclude that the amount of Ni dissolved in the ink is influenced by both its formulation and concentration. Interestingly, the reduction in the Ni fraction in the catalyst is further exacerbated after ink deposition using the ultrasonic spray coating technique, and even more so after MEA testing. The extent of Ni dissolution at each stage varies with the material under consideration. PtNi/C Sponge experiences the most significant Ni loss, partly due to its higher initial Ni content compared to other materials[36]. However, it's noteworthy that the Ni content post-testing is smallest for PtNi/C Octahedron, despite its initial content being similar to that of PtNi/C Sphere.

The ratio of Pt and Ni obtained from TEM-EDX is measured at low magnification on a whole carbon grain. Therefore, platinum and nickel present in the vicinity of the particle (on carbon or in the ionomer) are considered in this ratio. As presented in dedicated studies[27,30] and proven by the EDX mappings, dissolved Ni^{2+} cations quickly redistribute within the ionomer phase in the presence of humidity or heat. They are not expected to remain near the particle from which they originated, and the molar ratio measured on a zone close to the catalysts gives a good estimation of the ratio present in the alloyed particles. The total Ni loss and loading of SO_3^- moieties in the cathode active layer, calculated from the ionomer equivalent weight (EW) and the ionomer loading, are displayed in ***Figure 4b***. The total Ni loss and loading of SO_3^- moieties in the cathode active layer, calculated from the ionomer EW and the ionomer loading, are displayed in ***Figure 4b***. For PtNi/C Sponge, the quantity of Ni lost during the initial MEA stage is sufficient to replace all the protons of the ionomer with Ni^{2+} ions. However, as evidenced in specific studies, the released Ni^{2+} cations quickly redisperse within the entire ionomer phase, including the PEM[24,27,32], increasing the amount of SO_3^- to be poisoned at 3.2 $\mu mol_{SO3-}\ cm^{-2}$ (considering the properties of the PEM *i.e.* EW is 1100 mol g^{-1}, Volumic mass of 2.1 g cm^{-3}, thickness of 15 µm). Still, a large number of proton-conducting moieties are most likely poisoned by the presence of Ni^{2+} ions released from the cathode catalyst.

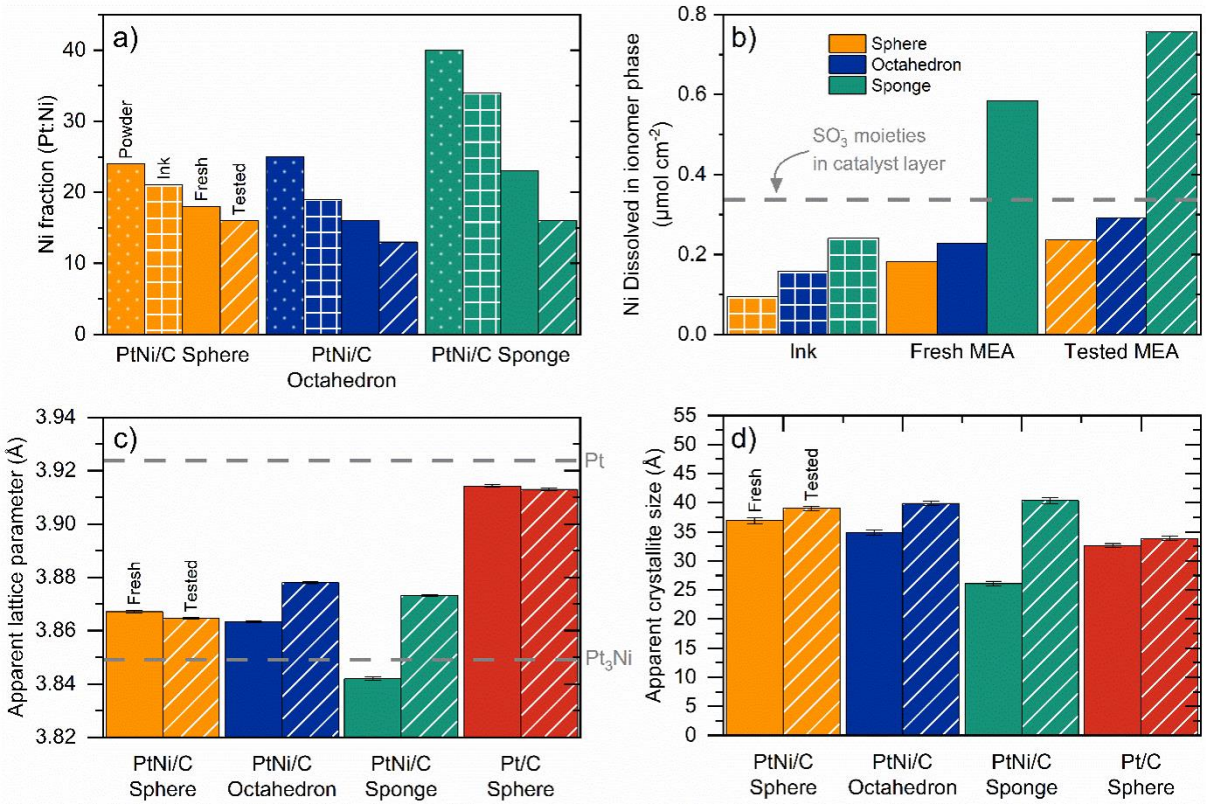

Figure 4 - a) Ni atomic fraction expressed in at%$_{metal}$ for the PtNi/C catalysts at different steps of their MEA integration calculated from EDX b) Corresponding total amount of Ni released in the ionomer phase after introduction of the PtNi/C catalysts in the ink, on the Fresh MEA and the Tested MEA. The dashed grey line indicates the loading of SO_3^- moieties of the ionomer in the active layer. The MEA$_{Symbio}$ were used for these measurements. c) Parameters extracted from X-ray Diffraction (XRD) patterns for a combination of the peaks from the alloy and from the pure Pt phase in the membrane and at the anode: Apparent lattice parameter extracted from the position of peak's maxima and d) Apparent crystallite size calculated from Sherrer's law. The MEA$_{ZSW}$ were used for XRD measurements.

The location of the dissolved nickel at the MEA scale is evaluated using energy-dispersive X-ray spectroscopy coupled with scanning electron microscopy (SEM-EDX). In ***Figure 5***, a direct comparison is made between Ni mappings for the PtNi/C Sponge Fresh and Tested MEAs. The mappings obtained for all the other materials are displayed in ***Supplementary Figure 7-9***. For all the PtNi/C catalysts, nickel is detected in the cathodic layer and the membrane. However, it does not contaminate the anodic layer. It is striking to note that the presence of nickel in the membrane is already clearly visible for the Fresh MEAs. The use of identical color scales for all MEAs allows for a comparison of the location of nickel in each case. After the test, the amount of nickel increases in the membrane but decreases in the cathodic layer. This trend is more visible for the PtNi/C Sponge but also present for PtNi/C Sphere and PtNi/C Octahedron.

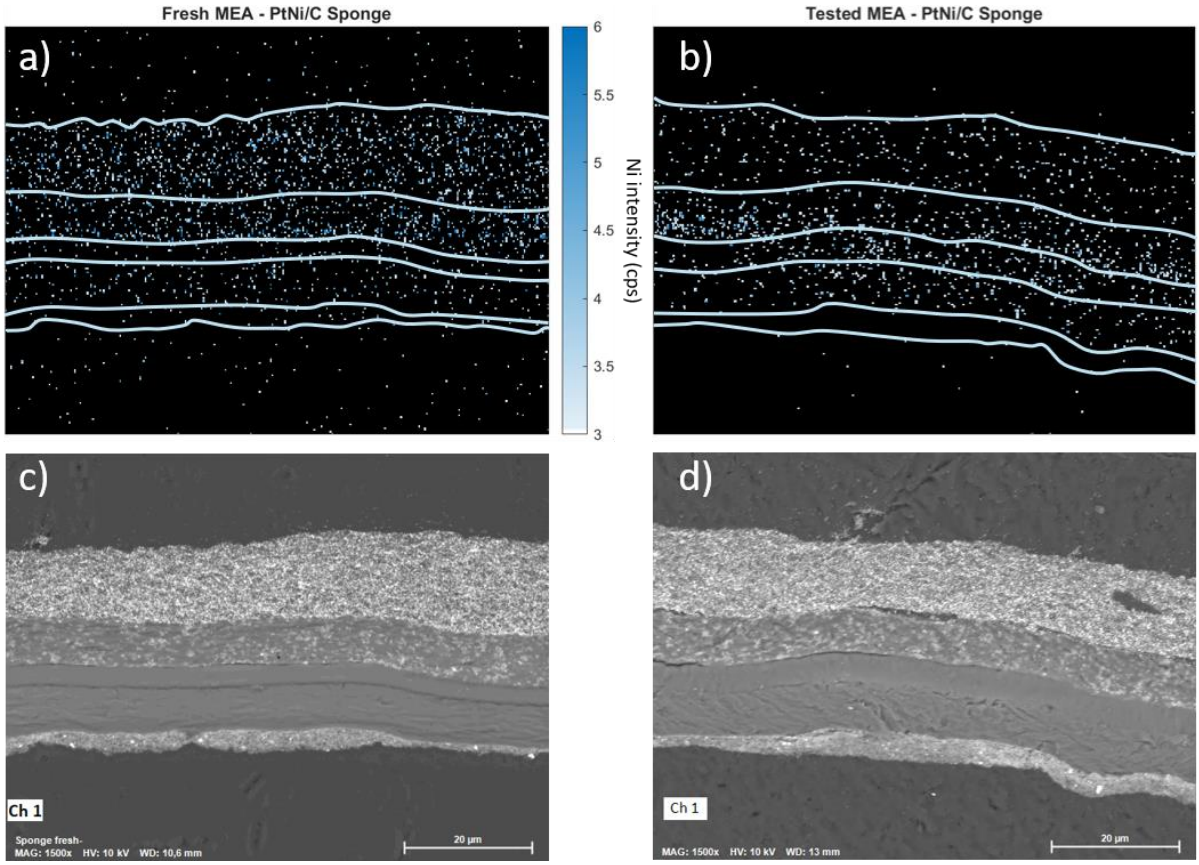

Figure 5 - Ni elemental maps of the MEA measured by SEM-EDX. a), c) for Fresh PtNi/C Sponge MEA_{Symbio} and b), d) for Tested PtNi/C Sponge MEA_{Symbio}. Delimitations of the boundaries of the PEM components have been drawn on the maps as visual aids.

The lattice parameter and the crystallite size of the particles were monitored using wide-angle X-ray scattering (WAXS) in transmission mode. The diffractograms are provided for each material in ***Supplementary Figure 10***. Note that the X-ray beam is diffracted by each component of the MEA presenting a crystalline structure: Cathode catalyst, Pt nanoparticles in the membrane (acting as scavengers), Teflon skeleton of the membrane, and Pt/C anodic catalytic layer. Given that both Pt and Pt_3Ni alloy crystallize in a face-centered cubic phase with close lattice parameters (3.85 Å and 3.92 Å for Pt_3Ni and Pt, respectively), the peaks corresponding to the cathode catalyst, anode catalyst, and Pt scavengers are convoluted in the diffractogram. However, it is reasonable to consider that at these early stages of the MEA's life, Pt located both in the PEM and at the anode remains unaltered. Therefore, any changes observed in peak position and shape during electrochemical testing were solely attributed to a change in the cathode catalyst layer. The calculated lattice parameter and crystallite size are presented in ***Figure 4c*** and ***Figure 4d***, respectively. These parameters are designated as "apparent", due to some contribution of the Pt particles present in the PEM and at the anode catalyst layer. For all

catalysts, the crystallite size increases slightly after testing. Consistent with observations from TEM images, this phenomenon is more pronounced for PtNi/C Octahedron and even more so for PtNi/C Sponge. The lattice parameter remains unchanged for Pt/C and PtNi/C Sphere despite the observed Ni loss in PtNi/C Sphere between Fresh and Tested MEAs. The Ni loss therefore does not significantly alter the degree of alloying in the bulk of the PtNi/C Sphere catalyst and seems to affect only the surface of this material. In contrast, for PtNi/C Sponge and Octahedron, the lattice parameter shifts towards smaller angles, indicating a relaxation of the lattice parameter. The significant Ni dissolution, monitored by TEM-EDX, leads to the formation of a Pt-richer alloy compared to the pristine ones.

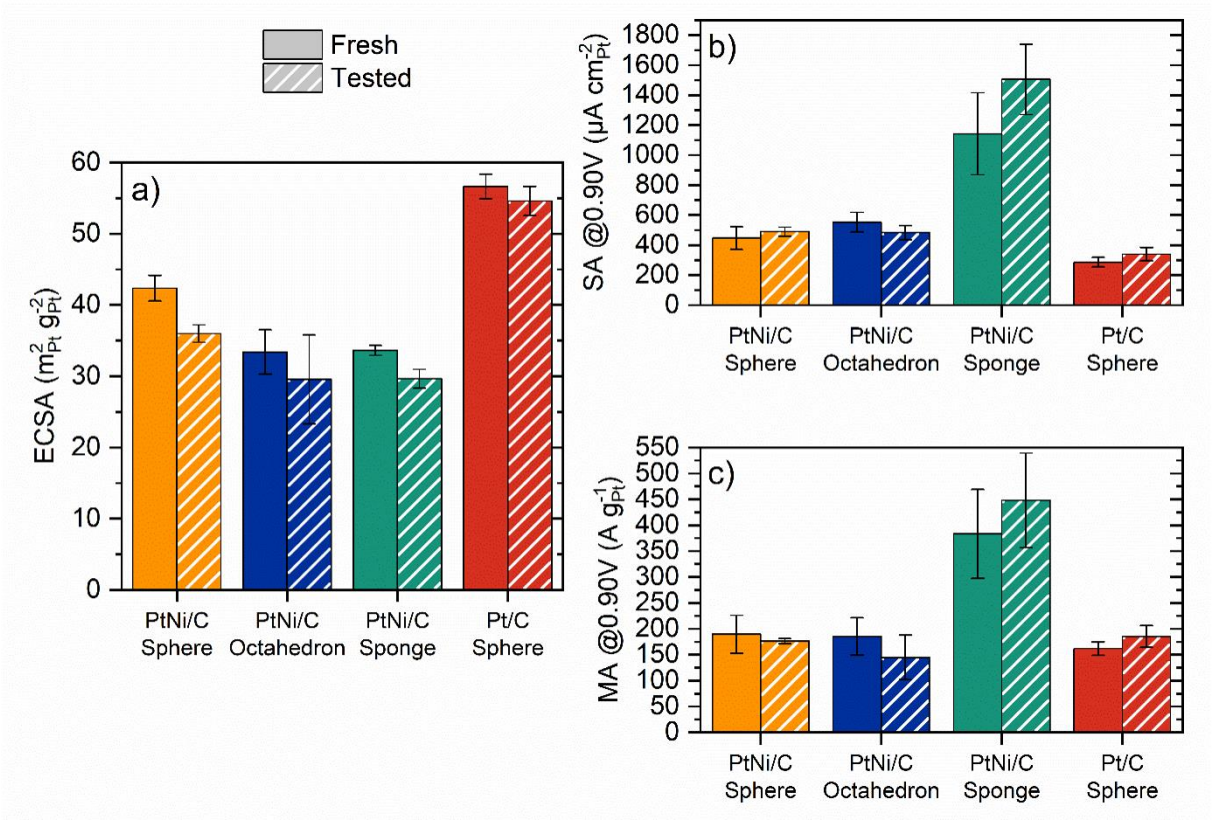

Figure 6 - Electrochemical performance measured in liquid electrolyte (25 °C, 0.1 M $HClO_4$, 1600 rpm, loading <25 μg_{Pt} cm^{-2}) for the scratched catalyst layer from a freshly prepared MEA (Fresh) and a tested MEA (Tested)from MEA_{Symbio}. a) Pt specific surface area calculated from Hydrogen under potential desorption (S_{Hupd}) normalized by Pt loading. b) Specific Activity i.e. current at E = 0.9 V_{RHE} normalized by S_{Hupd} and c) ORR Mass activity i.e. current at E = 0.9 V_{RHE} normalized by Pt loading.

In the first part of this manuscript, we have shown that the electrical performance of MEAs incorporating PtNi/C Octahedron and PtNi/C Sponge is impeded by the hydration of the ionomer in the catalyst layer, even at low current density. Therefore, quantitative assessment of

the EF, or any potential decrease of the intrinsic ORR activity of the catalyst in an MEA set-up is not absolute as it is influenced by the single-cell operating conditions applied (RH and O_2 stoichiometry). To analyze the evolution of the cathode catalyst catalytic activity, catalytic layers from Fresh and Tested MEAs were scratched away with a scalpel and formulated in ink for RDE (liquid electrolyte) characterization. The Pt specific surface area of all catalysts was estimated using the charge required for proton underpotential desorption (Hupd) (***Figure 6a***). The specific activity (SA) and mass activity (MA) for the ORR were determined from the kinetic current at E = 0.9 V, and their evolution upon MEA integration and electrochemical testing is illustrated in ***Figure 6*** for Fresh MEA and Tested MEA state. Between Fresh and Tested MEA electrode ECSA is significantly decreased for all the catalysts. These results agree with the crystallite size growth discussed in the previous paragraphs. The resulting ORR specific and mass activities are reported in ***Figure 6b*** and ***Figure 6c*** respectively. For PtNi/C Sphere, a slight decrease in ORR mass activity associated with nearly unchanged specific activity suggests that the intrinsic activities of the active sites remained unchanged and that the decrease in ORR mass activity is primarily due to crystallite growth. For PtNi/C Octahedron, the reduction in (111) facets presence observed in TEM images results in a slight decrease in ORR specific activity, approaching that of the PtNi/C Sphere. Conversely, for PtNi/C Sponge, the decrease in ECSA is counterbalanced by an important increase in the ORR specific activity.

Discussion

The monitoring of the particle's composition from the powder to the Tested MEA allowed to establish that Ni loss occurs as soon as the PtNi/C catalysts are formulated in ink. The dissolution occurs for every catalyst at each stage, but with varying intensity depending on particle shape, in agreement with what we recently reported using online ICP-MS [36]. All PtNi/C catalysts undergo significant changes in Ni content during integration into MEA and initial electrochemical testing but more pronounced alterations were observed for the two most active materials: PtNi/C Octahedra and PtNi/C Sponge. The dissolution of Ni cations starts as early as the ink preparation stage and results in cationic contamination of the ionomer phase, a phenomenon previously documented for aged MEAs and with conventional spherical Pt-alloy catalysts[23–28]. As suggested in reference [26,29], Ni^{2+} coordinates with two SO_3^- of the side chains of the ionomer, which makes the O_2 transport pathway torturous and hinders the transport of H^+. The fuel-cell results indicate that the ORR activity of the two best-performing materials (PtNi/C Octahedron and PtNi/C Sponge) is constrained by the hydration of the cathode catalyst layer. It was reported in reference[27], that decreased water uptake of the ionomer caused by

cationic contamination can generate the observed influence of RH on performance. The ionomer affects membrane hydration at low current densities: when minimal water is produced, and hydration becomes a limiting factor for these two catalysts unless the RH is sufficiently high[34]. For Sponge PtNi/C, ionomer hydration may be even more crucial as the pores of the particles may not be directly accessible to the ionomer. The amount of Ni dissolved for each material is in line with the relative current drops that are observed at higher current densities for the four materials in the polarization curves. In durability studies for alloyed catalysts, this effect was already associated with the contamination of the ionomer by the leached transition metal[23,25,26,29,40]. Here, this behavior is reported as soon as the very beginning of life and is expected to worsen with aging. This contamination of the ionomer phase layer by the dissolved Ni^{2+} is significantly larger for PtNi/C Sponge than for the MEAs embedding the two other PtNi/C catalysts, leading to a larger hindering of the O_2 transport pathway and the H^+ conduction through the ionomer thin film. In consequence, this results in the highest R_{O2} and R_{H+} for the MEA embedding PtNi/C Sponge, see ***Figure 2c and Figure 2d***, and the larger performance drop at high current loads, see ***Figure 1b***.

Therefore, it appears that during the early stage of the MEA fabrication, both facetted and disordered particles lose nickel that is rapidly homogenized in the membrane phase, polluting the ionomer while increasing their crystallite size and losing their preferential shape. However, it is well-established that larger crystallites tend to enhance the ORR specific activity[41], and our group has previously shown that the benefits of structural defects are partly maintained upon agglomeration of the crystallite for the PtNi/C Sponge[42]. These combined influences account for the rise in intrinsic ORR mass activity for the PtNi/C Sponge upon incorporation in the MEA. For PtNi/C Octahedron, the loss of facets causes a drop in intrinsic ORR activity. However, in both cases, the kinetic advantage of these materials is preserved, indicating that Ni cation contamination of the ionomer is the primary cause of the decreased performance observed at low current density in addition to being highly detrimental at high current density. The rapid occurrence of this degradation mechanism partly accounts for the performance gap when integrating highly active ORR catalysts (in this study, PtNi/C Sponge and PtNi/C Octahedra) into MEAs despite promising performance in liquid electrolyte. Since dissolution of the transition metal is the main contributor to the challenging transfer of highly active ORR catalysts in MEA, it is likely that similar results would be obtained for PtCo/C electrocatalysts, Co dissolution being largely documented in the literature[23–28].

Conclusions

In this study, membrane electrode assemblies were fabricated using highly active PtNi/C catalysts exhibiting two distinct morphologies: ordered/faceted and disordered/defective nanoparticles. We report the changes in shape, chemical composition, and ORR activity of these catalysts during the early stages of the MEA's life, from powder synthesis to initial electrochemical testing. All PtNi/C electrocatalysts experienced a notable loss of Ni during ink formulation and at each subsequent stage of the process (fresh MEA manufacturing, break-in, and electrochemical testing). The faceted structure of the PtNi/C Octahedron transitioned towards a spherical morphology, resulting in an ORR specific activity comparable to that of the reference PtNi/C Sphere. PtNi/C Sponges, initially possessing smaller crystallite sizes, exhibited crystallite growth leading to increased ORR specific activity and subsequent mass activity despite a reduction in electrochemically active surface area. These changes in composition and shape did not significantly impact the catalyst performance at low current densities in the MEA. Nevertheless, for all Ni-containing catalysts, the release of Ni into the ionomer phase significantly hindered O_2 transport properties, nullifying any advantages over Pt/C catalysts at current densities exceeding 1 A cm^{-2}_{geo}. We thus conclude that spherical PtNi/C submitted to harsh acid leaching prior or post MEA manufacturing should offer the best compromise to mitigate this adverse effect.

Acknowledgments

We thank Marta Mirolo from the ID31 beamline of the European Synchrotron Radiation Facility (ESRF) for her help with WAXS diffractograms acquisition.

This work was supported by the French National Research Agency in the frame of the BRIDGE project (grant number ANR-19-ENER-0008-01). MSR and SB acknowledge the financial support from the German Federal Ministry of Education and Research in the frame of the project BRIDGE (grant number 03SF0585).

References

1. P. Mani, R. Srivastava, and P. Strasser, *J. Phys. Chem. C*, **112**, 2770–2778 (2008).

2. R. Chattot, T. Asset, P. Bordet, J. Drnec, L. Dubau, and F. Maillard, *ACS Catal.*, **7**, 398–408 (2017).

3. V. R. Stamenkovic, B. Fowler, B. S. Mun, G. Wang, P. N. Ross, C. A. Lucas, and N. M. Marković, *Science*, **315**, 493–497 (2007).

4. V. R. Stamenkovic, B. S. Mun, K. J. J. Mayrhofer, P. N. Ross, and N. M. Markovic, *J. Am. Chem. Soc.*, **128**, 8813–8819 (2006).

5. J. R. Kitchin, J. K. Nørskov, M. A. Barteau, and J. G. Chen, *Phys. Rev. Lett.*, **93**, 156801 (2004).

6. T. Asset, R. Chattot, M. Fontana, B. Mercier-Guyon, N. Job, L. Dubau, and F. Maillard, *Chemphyschem Eur. J. Chem. Phys. Phys. Chem.*, **19**, 1552–1567 (2018).

7. C. Cui, L. Gan, M. Heggen, S. Rudi, and P. Strasser, *Nat. Mater.*, **12**, 765–771 (2013).

8. R. Chattot, O. Le Bacq, V. Beermann, S. Kühl, J. Herranz, S. Henning, L. Kühn, T. Asset, L. Guétaz, G. Renou, J. Drnec, P. Bordet, A. Pasturel, A. Eychmüller, T. J. Schmidt, P. Strasser, L. Dubau, and F. Maillard, *Nat. Mater.*, **17**, 827–833 (2018).

9. S. Kühl, M. Gocyla, H. Heyen, S. Selve, M. Heggen, R. E. Dunin-Borkowski, and P. Strasser, *J. Mater. Chem. A*, **7**, 1149–1159 (2019).

10. P. Strasser, M. Gliech, S. Kuehl, and T. Moeller, *Chem. Soc. Rev.*, **47**, 715–735 (2018).

11. J. Choi, Y. Lee, J. Kim, and H. Lee, *J. Power Sources*, **307**, 883–890 (2016).

12. X. Huang, Z. Zhao, L. Cao, Y. Chen, E. Zhu, Z. Lin, M. Li, A. Yan, A. Zettl, Y. M. Wang, X. Duan, T. Mueller, and Y. Huang, *Science*, **348**, 1230–1234 (2015).

13. J. Wu, L. Qi, H. You, A. Gross, J. Li, and H. Yang, *J. Am. Chem. Soc.*, **134**, 11880–11883 (2012).

14. M. K. Carpenter, T. E. Moylan, R. S. Kukreja, M. H. Atwan, and M. M. Tessema, *J. Am. Chem. Soc.*, **134**, 8535–8542 (2012).

15. X. Wang, L. Figueroa-Cosme, X. Yang, M. Luo, J. Liu, Z. Xie, and Y. Xia, *Nano Lett.*, **16**, 1467–1471 (2016).

16. M. Li, Z. Zhao, T. Cheng, A. Fortunelli, C.-Y. Chen, R. Yu, Q. Zhang, L. Gu, B. V. Merinov, Z. Lin, E. Zhu, T. Yu, Q. Jia, J. Guo, L. Zhang, W. A. Goddard, Y. Huang, and X. Duan, *Science*, **354**, 1414–1419 (2016).

17. O. Le Bacq, A. Pasturel, R. Chattot, B. Previdello, J. Nelayah, T. Asset, L. Dubau, and F. Maillard, *ChemCatChem*, **9**, 2324–2338 (2017).

18. R. Chattot, I. Martens, M. Scohy, J. Herranz, J. Drnec, F. Maillard, and L. Dubau, *ACS Energy Lett.*, **5**, 162–169 (2020).

19. J.-H. Byeon, D.-H. Park, W.-J. Lee, M.-H. Kim, H.-J. Lee, and K.-W. Park, *J. Power Sources*, **556**, 232483 (2023).

20. X. Peng, S. Zhao, T. J. Omasta, J. M. Roller, and W. E. Mustain, *Appl. Catal. B Environ.*, **203**, 927–935 (2017).

21. D. D. Papadias, R. K. Ahluwalia, N. Kariuki, D. Myers, K. L. More, D. A. Cullen, B. T. Sneed, K. C. Neyerlin, R. Mukundan, and R. L. Borup, *J. Electrochem. Soc.*, **165**, F3166

(2018).

22. X. Wang, L. Hu, K. C. Neyerlin, and R. K. Ahluwalia, *J. Electrochem. Soc.*, **170**, 024503 (2023).

23. Y. Cai, A. Kongkanand, W. Gu, and T. E. Moylan, *ECS Trans.*, **69**, 1047 (2015).

24. N. Ramaswamy, S. Kumaraguru, W. Gu, R. S. Kukreja, K. Yu, D. Groom, and P. Ferreira, *J. Electrochem. Soc.*, **168**, 024519 (2021).

25. M. Gatalo, A. M. Bonastre, L. J. Moriau, H. Burdett, F. Ruiz-Zepeda, E. Hughes, A. Hodgkinson, M. Šala, L. Pavko, M. Bele, N. Hodnik, J. Sharman, and M. Gaberšček, *ACS Appl. Energy Mater.*, **5**, 8862–8877 (2022).

26. J. P. Braaten, X. Xu, Y. Cai, A. Kongkanand, and S. Litster, *J. Electrochem. Soc.*, **166**, F1337 (2019).

27. C. Lee, X. Wang, J.-K. Peng, A. Katzenberg, R. K. Ahluwalia, A. Kusoglu, S. Komini Babu, J. S. Spendelow, R. Mukundan, and R. L. Borup, *ACS Appl. Mater. Interfaces*, **14**, 35555–35568 (2022).

28. R. K. Ahluwalia, X. Wang, J.-K. Peng, N. N. Kariuki, D. J. Myers, S. Rasouli, P. J. Ferreira, Z. Yang, A. Martinez-Bonastre, D. Fongalland, and J. Sharman, *J. Electrochem. Soc.*, **165**, F3316–F3327 (2018).

29. J. Durst, M. Chatenet, and F. Maillard, *Phys. Chem. Chem. Phys.*, **14**, 13000 (2012).

30. R. K. Ahluwalia, D. D. Papadias, N. N. Kariuki, J.-K. Peng, X. Wang, Y. Tsai, D. G. Graczyk, and D. J. Myers, *J. Electrochem. Soc.*, **165**, F3024–F3035 (2018).

31. M. Tesfaye and A. Kusoglu, *ECS Trans.*, **86**, 359 (2018).

32. B. L. Kienitz, H. Baskaran, and T. A. Zawodzinski, *Electrochimica Acta*, **54**, 1671–1679 (2009).

33. T. A. Greszler, T. E. Moylan, and H. A. Gasteiger, in *Handbook of Fuel Cells*,, John Wiley & Sons, Ltd (2010) https://onlinelibrary.wiley.com/doi/abs/10.1002/9780470974001.f500049.

34. C. Bas, L. Flandin, A.-S. Danerol, E. Claude, E. Rossinot, and N. D. Alberola, *J. Appl. Polym. Sci.*, **117**, 2121–2132 (2010).

35. S. Chen, H. A. Gasteiger, K. Hayakawa, T. Tada, and Y. Shao-Horn, *J. Electrochem. Soc.*, **157**, A82 (2009).

36. C. Roiron, V. Martin, K. Kumar, L. Dubau, and F. Maillard, *Electrochimica Acta*, **477**, 143760 (2024).

37. M. Lee, M. Uchida, H. Yano, D. A. Tryk, H. Uchida, and M. Watanabe, *Electrochimica Acta*, **55**, 8504–8512 (2010).

38. L. Dubau, L. Guétaz, J. Durst, F. Maillard, M. Chatenet, J. André, and E. Rossinot, *ECS*

Electrochem. Lett., **1**, F13 (2012).

39. T. Mashio, A. Ohma, S. Yamamoto, and K. Shinohara, *ECS Trans.*, **11**, 529 (2007).

40. T. Okada, Y. Ayato, H. Satou, M. Yuasa, and I. Sekine, *J. Phys. Chem. B*, **105**, 6980–6986 (2001).

41. K. Kinoshita, *J. Electrochem. Soc.*, **137**, 845 (1990).

42. L. Dubau, J. Nelayah, T. Asset, R. Chattot, and F. Maillard, *ACS Catal.*, **7**, 3072–3081 (2017).

Figure Captions

Figure 1

a) Transmission electron microscopy images from the library of materials used in this study with same magnification, b) Low current zoom-in of 25 cm² MEA polarization curve recorded at 80 C, 100% RH, 1.5barg in H_2/Air, c) Mass activity of the catalyst at 0.9 V in RDE and MEA set-up (recorded at 80 °C, 100% RH, 1.5barg in H_2/Air) averaged over the two sets of measurements. d) Enhancement Factor (EF) vs. benchmark Pt/C Sphere catalyst in each set-up: ORR mass activity of the catalyst at 0.9 V divided by that of the Pt/C reference catalyst for both MEA and liquid electrolyte (RDE) characterization (RDE at 25 °C, 1600 rpm in 0.1 M $HClO_4$ and MEA at 80 °C and 1.5 barg).

Figure 2

a) Power density recorded at U = 0.9 V as a function of the cathode relative humidity b) Power density recorded at 1.5 A cm^{-2}_{geo} as a function of the oxygen stoichiometry at 1 A cm^{-2} for the MEA_{ZSW} c) Pressure-dependent and pressure-independent oxygen transport resistance measured at 80 °C, 100 % RH and d) Proton transport resistance measured for each MEA at the end of the test under H_2/N_2 (anode/cathode) at 60% RH, 80 °C - Evolution of PEMFC performance during two types of activation procedures. e) For MEA_{ZSW}: 10 min current steps at 12 and 16 A (0.48 and 0.64 A cm^{-2}) applied for 322 min and f) For MEA_{Symbio}: Potential hold at 0.7 V for 120 min.

Figure 3

Transmission electron microscopy images in the pristine powder state (Powder), after deposition on the PEM (Fresh MEA) and after beginning-of-life testing (Tested MEA) of the MEA_{Symbio}.

Figure 4

a) Ni atomic fraction expressed in $at\%_{metal}$ for the PtNi/C catalysts at different steps of their MEA integration calculated from EDX b) Corresponding total amount of Ni released in the ionomer phase after introduction of the PtNi/C catalysts in the ink, on the Fresh MEA and the Tested MEA. The dashed grey line indicates the loading of SO_3^- moieties of the ionomer in the active layer. The MEA_{Symbio} were used for these measurements. c) Parameters extracted from X-ray Diffraction (XRD) patterns for a combination of the peaks from the alloy and from the pure Pt phase in the membrane and at the anode: Apparent lattice parameter extracted from the position of peak's maxima and d) Apparent crystallite size calculated from Sherrer's law. The MEA_{ZSW} were used for XRD measurements.

Figure 5

Ni elemental maps comparing the Fresh and Tested PtNi/C Sponge MEA_{Symbio}. Delimitations of the boundaries of the PEM membrane have been drawn as visual aids.

Figure 6

Electrochemical performance measured in liquid electrolyte (25 °C, 0.1 M $HClO_4$, 1600 rpm, loading <25 μg_{Pt} cm^{-2}) for the scratched catalyst layer from a freshly prepared MEA (Fresh) and a tested MEA (Tested)from MEA_{Symbio}. a) Pt specific surface area calculated from

Hydrogen under potential desorption (S_{Hupd}) normalized by Pt loading. b) Specific Activity i.e. current at E = 0.9 V_{RHE} normalized by S_{Hupd} and c) ORR Mass activity i.e. current at E = 0.9 V_{RHE} normalized by Pt loading.